Theoretical and Applied Fracture Mechanics 124 (2023) 103753

Contents lists available at ScienceDirect

Theoretical and Applied Fracture Mechanics

journal homepage: www.elsevier.com/locate/tafmec

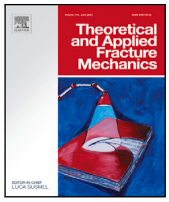

A developed hybrid experimental–analytical method for thermal stress analysis of a deep U-notched plate

Abdullah A. Alshaya

Mechanical Engineering Department, College of Engineering and Petroleum, Kuwait University, P.O. Box 5969, Safat 13060, Kuwait

ARTICLE INFO

Keywords:
Michell solution
Thermoelastic stress analysis
Stress concentration
Airy stress function
Elastostatics
Linear elasticity

ABSTRACT

A general framework of hybridizing experimentally-recorded load-induced thermal information by means of thermoelastic stress analysis (TSA) of a loaded structure with the Michell solution of Airy stress function in isotropic linear elasticity is proposed for in-plane stresses determination. The capability of the proposed hybrid method in separating the TSA signals into individual stresses is demonstrated by stress-analyzing a deep U-notched aluminum plate without neither knowing the entire geometry and distant loading/boundary conditions nor using supplementary experimental information. Even though no experimental data were processed at, and adjacent to, the edges of the U-notched plate, the individual stresses are determined throughout the surface of the plate. Prior processing actual experimental TSA data, the accuracy and the stability of the proposed hybrid method through adding artificial noise scatters in the processed simulated data with the number of retained terms in the generalized Airy stress expressions are firstly investigated. The effects of the superimposed noise scatters as well as the number of employed data in the evaluated stresses are also assessed. Finally, the reliability of the determined hybrid-experimental stresses is supported through a comparison with finite-element predictions and strain gauge measurements. The ease of implementation, the accuracy and the precision of the evaluated stress, and the versatility to the type of employed data make the proposed hybrid method more attractive and superior than other hybrid methods.

1. Introduction

Fracture and yield prevention as well as fatigue-life prediction necessitate the determination of the full-field stresses in loaded structures. The stresses-evaluation approaches based on analytical methods and numerical techniques are limited to simple geometries and structures with well-defined external loading and boundary conditions (which usually are unavailable in practice) [1–5]. Hence, experimental mechanics techniques are commonly used to capture the exact effects of the loading and boundary conditions [6–8]. However, experimental data in the proximity of edges are usually unavailable or even unreliable especially if the considered structure has abrupt internal geometric discontinuities. The high stresses in the locality of these geometric cutouts can significantly influence the structural reliability [9,10]. The displacement-based experimental techniques such as moiré interferometry, digital speckle pattern interferometry, and digital image correlation (DIC), require a priori knowledge of material elastic coefficients and spatial numerical differentiation in order to relate the deformation with the failure parameters. Furthermore, experimental techniques that are based on measuring load-induced information that are related to the changes in stresses such as strain gauges, thermoelastic stress analysis (TSA) and photoelastic stress analysis (PSA) require supplementary experiment and/or numerical analysis to extract the individual stresses components [11–16]. Therefore, hybrid methods are commonly used to couple the experimental information with a numerical or an analytical tool (or both) to solve the aforementioned situations in each of the individual experimental techniques [17–19].

Thermoelastic stress analysis (TSA) is commonly used to stress-analyze loaded structures by utilizing an infrared camera to record thermal information that are related under adiabatic condition to the changes in the mechanical stresses [20–27]. Even through PSA and strain gauges provide load-induced information as the TSA technique does, the former require time-consuming installation and nonlinear numerical analysis to obtain the individual stresses where the latter provides the experimental results within minutes and require linear analysis. The idea of hybridizing analytical and/or numerical analyses with the thermal information is to make TSA as a quantitative, not just a qualitative, engineering tool [28].

Cracks are commonly initiated from a side notch which characterizes the integrity of a loaded structure. For instance, Ermin et al. [29] and Shuai et al. [30] hybridized Williams series approximation and theoretical field with DIC displacement measurements in order to characterize the stress intensity factor (SIF) of crack initiated from a sided

E-mail address: abdullah.alshaye@ku.edu.kw.

https://doi.org/10.1016/j.tafmec.2023.103753
Received 23 November 2022; Received in revised form 22 December 2022; Accepted 5 January 2023
Available online 14 January 2023

Nomenclature

ASF	Airy Stress Function
$\mathbf{d}^*$	Vector of numerical values of processing data and boundary conditions
$\mathbf{d}_{\text{Airy}}$	Vector of reconstructed values of $\mathbf{d}^*$ by means of hybrid-ASF method
E and ν	Young's modulus and Poisson's ratio
F	Applied concentrated tensile load
h	Number of employed tractions and/or displacements conditions
k	Number of determined Airy coefficients in ASF, Φ
K	TSA calibration factor
L	Plate half-thickness
m	Number of employed TSA data
n_x and n_y	Outward unit normals to the body surface
N	Terminating index of the summation series in ASF
$\mathcal{N}(0,\gamma)$	Standard Gaussian function with 0-mean and γ-standard-deviation
r,θ	Polar coordinates
R	Radius of a deep U-notch
R^*	Region of processing measured data in hybrid-ASF method
S	Isopachic stress, $S=\sigma_{xx}+\sigma_{yy}=\sigma_{rr}+\sigma_{\theta\theta}$
S^*	Load-induced thermal information, i.e., TSA signals
t_x and t_y	Surface tractions with respect to a unit area
$\bar{T}_x$ and $\bar{T}_y$	Prescribed plane tractions
TSA	Thermoelastic Stress Analysis
$\bar{u}$ and $\bar{v}$	Prescribed in-plane displacements
x,y,z	Cartesian (rectangular) coordinates
α and β	Summation convention in two dimensions (x,y), (r,θ), or $(1,2)$
Γ_u and Γ_t	Boundaries with prescribed displacements and tractions
$\delta_{\alpha\beta}$	Kronecker delta
λ and μ	Lamè constants
$\sigma_{\alpha\beta}$, $\epsilon_{\alpha\beta}$, and u_α	In-plane stresses, strains, and displacements
σ_{rr}, $\sigma_{\theta\theta}$, and $\sigma_{r\theta}$	In-plane polar stresses
σ_{xx}, σ_{yy}, and σ_{xy}	In-plane Cartesian stresses
Φ	Airy stress function
Ω and $\partial\Omega$	Domain and boundary of a two-dimensional loaded solid elastic body
∇^2	Plane Laplacian operator

U-notched plate. Thermography was also used to determine SIF and predict the fatigue crack propagation in loaded notched plates [31–36]. Several empirical formulas for stress concentration factor (SCF) and published literature information are available for single- or double-edge notches [10,37–43], but little appears to be available for a deep U-notch. Therefore, it is necessary to know the stress field around a sided U-notched plate in order to prevent the initiation of a crack, and hence, prevent sudden fracture of the engineering structure.

The plane elasticity solution of a loaded linear isotropic member assuming no body forces can be obtained from the biharmonic equation in terms of the Airy stress function (ASF). The general solution for such equation is known as the Michell solution [5]. Analytical applications of the Michell solution to numerous elasticity problems including mixed boundary value problems are available in [44–49]. One of the well-established hybrid method is based on using the Michell general solution as the analytical ingredient of the hybrid method [28,50]. Unlike the analytical approach of determining the unknown coefficients of the ASF from the boundary condition, the hybrid method is based on determining these coefficients from processing experimental data and satisfying some of the known boundary conditions. Unlike numerical and analytical approaches, the hybrid-ASF method satisfies the equilibrium and compatibility conditions in their strong forms by utilizing the ASF, and captures the effects of the external loading and distant boundary conditions by processing experimental information. This helps the proposed hybrid method to filter out the noises incorporated in the experimental data and overcome the traditional difficulties of unreliable edge data.

The hybrid-ASF method was previously tested for diametrically-loaded disk [51] and axially-loaded plates with different internal geometrical discontinuities, e.g., circular [52,53], elliptical [54,55], and arbitrarily-shaped [56] holes, while processing experimental data in the form of load-induced TSA information [51,52,54,56] and DIC displacement measurements [53,55]. The method was then extended to stress-analyze unsymmetrically-loaded plate with circular [57], elliptical [58], and arbitrarily-shaped [59] holes. By using thermoelasticity and hybrid-ASF, Samad et al. [60] stress-analyzed a pin-loaded plate and Lin et al. [61,62] separated the TSA signals of a loaded square plate with a near-edge hole into the individual stresses. The full-field individual stresses in a pinned wooden joint were obtained from gray-field photoelasticity and hybrid-ASF [63]. Kalayciogli et al. determined the experimental stresses of a concentrated-loaded finite structure with arbitrarily- and irregularly-shaped exterior geometry and interior discontinuity using TSA [64] and DIC [65] measurements. The complex representation of the ASF with analytic continuation and conformal mapping was also used to stress-analyze loaded anisotropic structures having traction-free geometric discontinuities using strain gauge [66], moirè [67], PSA [68], TSA [38,69–71], and DIC [39] measurements. However, the enforcement of the analytic continuation principle requires traction-free boundaries unlike the present approach that is applicable to loaded- and free-boundaries.

All of the previous applications of the hybrid-ASF method were based on a coordinate system that is enclosed by the domain of the loaded structure. These scenarios simplify the form of the Michell general solution by assuming single-valued stresses and displacements, symmetry along the horizontal and vertical axes and/or bounded stresses and displacement at origin or infinity. Unlike the results presented in [72], the main contribution of this paper is to extend the capability of the hybrid-ASF method by utilizing the full form of the ASF to stress-analyze a loaded finite aluminum plate with a single deep U-notch whose coordinate system lies outside its domain. The advantageous of processing surface temperature measurements from TSA is to capture the exact loading conditions, while the traction-free boundaries at the edges were discretely imposed in order to provide reliable full-field stresses at and in the neighborhood of the deep U-notch. The stability of the proposed hybrid-ASF method was tested through numerical simulation by artificially deteriorating the processed simulated thermoelastic signal data, and its reliability was demonstrated through experimental verification by means of TSA technique. The accuracy of the proposed method in determination of the in-plane stresses with the number of retained terms in the expression of the Airy solution while processing different set of data (based on its size and noise-level) are investigated. The reliability of the hybrid-experimental results is supported through a comparison with finite-element predictions and strain gauge measurements.

2. Airy stress function (Michell solution)

2.1. Theory of plane elasticity

A two-dimensional loaded solid elastic body defined by a domain Ω and enclosed by a boundary $\partial\Omega$ is considered, Fig. 1. Although many

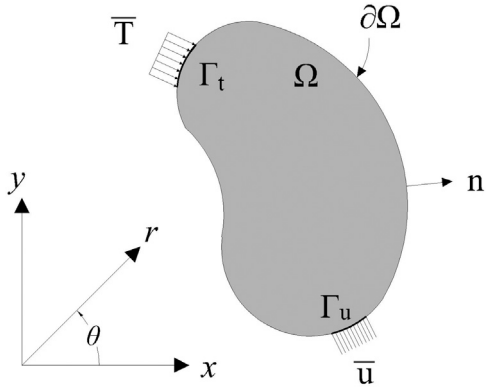

Fig. 1. Elastic solid body in a two-dimensional space.

stress analyses situations are really three dimensional in nature, when possible it is convenient to assume plane-stress or plane-strain. The basic equations of plane elasticity in isotropic medium with the absence of the body forces are given as

$$\sigma_{\alpha\beta,\alpha} = 0 \tag{1a}$$

$$\epsilon_{\alpha\beta} = \frac{1}{2}\left(u_{\alpha,\beta} + u_{\beta,\alpha}\right) \tag{1b}$$

$$\sigma_{\alpha\beta} = \lambda\delta_{\alpha\beta}\epsilon_{kk} + 2\mu\epsilon_{\alpha\beta} \tag{1c}$$

where $\sigma_{\alpha\beta}$, $\epsilon_{\alpha\beta}$, and u_α are the in-plane stresses, strains, and displacements, the Greek subscripts α and β imply the summation convention in two dimensions, subscript "$,i$" denotes a partial derivative with respect to the spatial coordinate i, λ and μ are the Lamè constants, and $\delta_{\alpha\beta}$ is the Kronecker delta. The portions of the supported and loaded boundaries are denoted by Γ_u and Γ_t, respectively. Therefore, the displacement (essential) and tractions (natural) boundary conditions on the boundaries Γ_u and Γ_t, respectively, can be written as follows

$$t_x = \sigma_{xx}n_x + \sigma_{xy}n_y = \bar{T}_x \quad \text{and} \quad t_y = \sigma_{xy}n_x + \sigma_{yy}n_y = \bar{T}_y \quad \text{on } \Gamma_t \tag{2a}$$

$$u = \bar{u} \quad \text{and} \quad v = \bar{v} \quad \text{on } \Gamma_u \tag{2b}$$

where t_x and t_y are the surface traction (or load) with respect to a unit area, $n_x = \cos(\mathbf{n}, \mathbf{x})$ and $n_y = \cos(\mathbf{n}, \mathbf{y})$ are the outward unit normals to the surface of the body, σ_{xx}, σ_{yy}, and σ_{xy} are the normal and shear stresses in the xy-plane, u and v are the in-plane displacement components along the global coordinates, x- and y-axes, respectively. $\bar{u}$ and $\bar{v}$ and $\bar{T}_x$ and $\bar{T}_y$ are the prescribed displacements and traction (externally-applied loads) on the boundary regions Γ_u and Γ_t, respectively. The traction-free boundary with no displacement or load enforcement can be viewed as the extension of Γ_t. It is worth noting that $\Gamma_t \cup \Gamma_u = \partial\Omega$ and $\Gamma_t \cap \Gamma_u = \emptyset$.

2.2. Michell solution

For elastostatic plane problems governed in the domain space Ω, the stress equilibrium, Eq. (1a), is identically satisfied by introducing the Airy stress function Φ where the imposing of the strains compatibility condition, from Eq. (1b), gives the following biharmonic equation,

$$\nabla^4\Phi = \nabla^2\nabla^2\Phi = \left(\frac{\partial^2}{\partial x^2} + \frac{\partial^2}{\partial y^2}\right)^2\Phi = \left(\frac{\partial}{\partial r^2} + \frac{1}{r}\frac{\partial}{\partial r} + \frac{1}{r^2}\frac{\partial}{\partial\theta^2}\right)^2\Phi = 0 \tag{3}$$

where ∇^2 is the Laplacian operator defined in the plane Cartesian and polar coordinate systems. The general solution, known as Michell solution, of Eq. (3) in polar coordinates with θ-dependence and periodic in nature is given as [5]

$$\begin{aligned}\Phi(r,\theta) = {} & a_0 + b_0\ln r + c_0 r^2 + d_0 r^2\ln r + \left(A_0 + B_0\ln r + C_0 r^2 + D_0 r^2\ln r\right)\theta \\ & + \left(a_1 r + b_1 r\ln r + \frac{c_1}{r} + d_1 r^3\right)\sin\theta \\ & + \left(a_1' r + b_1' r\ln r + \frac{c_1'}{r} + d_1' r^3\right)\cos\theta \\ & + \left(A_1 r + B_1 r\ln r\right)\theta\sin\theta + \left(A_1' r + B_1' r\ln r\right)\theta\cos\theta \\ & + \sum_{n=2,3,..}^{N}\left(a_n r^n + b_n r^{n+2} + c_n r^{-n} + d_n r^{-(n-2)}\right)\sin(n\theta) \\ & + \sum_{n=2,3,..}^{N}\left(a_n' r^n + b_n' r^{n+2} + c_n' r^{-n} + d_n' r^{-(n-2)}\right)\cos(n\theta)\end{aligned} \tag{4}$$

where r and θ are the radial and angular (measured counterclockwise from the positive x-axis) coordinates, Fig. 1, and N is the terminal index of the summation. The unknown constants, referred to as Airy coefficients, are evaluated from the boundary conditions, Eq. (2).

2.2.1. In-plane stresses

The individual components of polar stresses are evaluated from the Airy stress function as

$$\begin{aligned}&\sigma_{rr} = \frac{1}{r}\frac{\partial\Phi}{\partial r} + \frac{1}{r^2}\frac{\partial^2\Phi}{\partial\theta^2}, \qquad \sigma_{\theta\theta} = \frac{\partial^2\Phi}{\partial r^2}, \\ &\sigma_{r\theta} = -\frac{\partial}{\partial r}\left(\frac{1}{r}\frac{\partial\Phi}{\partial\theta}\right) = \frac{1}{r^2}\frac{\partial\Phi}{\partial\theta} - \frac{1}{r}\frac{\partial^2\Phi}{\partial r\partial\theta}\end{aligned} \tag{5}$$

Therefore from Eqs. (4) and (5), the individual components of stresses are

$$\begin{aligned}\sigma_{rr} = {} & \frac{b_0}{r^2} + 2c_0 + d_0(2\ln r + 1) + B_0\frac{\theta}{r^2} + 2C_0\theta + D_0(2\ln r + 1)\theta \\ & + \left(\frac{b_1}{r} - \frac{2c_1}{r^3} + 2d_1 r\right)\sin\theta + \left(\frac{b_1'}{r} - \frac{2c_1'}{r^3} + 2d_1' r\right)\cos\theta \\ & + \frac{2A_1}{r}\cos\theta + \frac{B_1}{r}(\theta\sin\theta + 2\ln r\cos\theta) \\ & - \frac{2A_1'}{r}\sin\theta + \frac{B_1'}{r}(\theta\cos\theta - 2\ln r\sin\theta) \\ & - \sum_{n=2,3,..}^{N}\Big[a_n n(n-1)r^{n-2} + b_n(n+1)(n-2)r^n \\ & \qquad + c_n n(n+1)r^{-(n+2)} + d_n(n-1)(n+2)r^{-n}\Big]\sin(n\theta) \\ & - \sum_{n=2,3,..}^{N}\Big[a_n' n(n-1)r^{n-2} + b_n'(n+1)(n-2)r^n \\ & \qquad + c_n' n(n+1)r^{-(n+2)} + d_n'(n-1)(n+2)r^{-n}\Big]\cos(n\theta)\end{aligned} \tag{6a}$$

$$\begin{aligned}\sigma_{\theta\theta} = {} & -\frac{b_0}{r^2} + 2c_0 + d_0(2\ln r + 3) - B_0\frac{\theta}{r^2} + 2C_0\theta + D_0(2\ln r + 3)\theta \\ & + \left(\frac{b_1}{r} + \frac{2c_1}{r^3} + 6d_1 r\right)\sin\theta + \left(\frac{b_1'}{r} + \frac{2c_1'}{r^3} + 6d_1' r\right)\cos\theta \\ & + \frac{B_1}{r}\theta\sin\theta + \frac{B_1'}{r}\theta\cos\theta \\ & + \sum_{n=2,3,..}^{N}\Big[a_n n(n-1)r^{n-2} + b_n(n+1)(n+2)r^n \\ & \qquad + c_n n(n+1)r^{-(n+2)} + d_n(n-1)(n-2)r^{-n}\Big]\sin(n\theta) \\ & + \sum_{n=2,3,..}^{N}\Big[a_n' n(n-1)r^{n-2} + b_n'(n+1)(n+2)r^n \\ & \qquad + c_n' n(n+1)r^{-(n+2)} + d_n'(n-1)(n-2)r^{-n}\Big]\cos(n\theta)\end{aligned} \tag{6b}$$

$$\begin{aligned}\sigma_{r\theta} = {} & \frac{A_0}{r^2} + B_0\frac{\ln r - 1}{r^2} - C_0 - D_0(\ln r + 1) \\ & + \left(-\frac{b_1}{r} + \frac{2c_1}{r^3} - 2d_1 r\right)\cos\theta - \left(-\frac{b_1'}{r} + \frac{2c_1'}{r^3} - 2d_1' r\right)\sin\theta\end{aligned}$$

$$
\begin{aligned}
&- \frac{B_1}{r}(\sin\theta + \theta\cos\theta) - \frac{B_1'}{r}(\cos\theta - \theta\sin\theta) \\
&- \sum_{n=2,3,..}^{N} \Big[a_n n(n-1) r^{n-2} + b_n n(n+1) r^{n} \\
&\qquad - c_n n(n+1) r^{-(n+2)} - d_n n(n-1) r^{-n} \Big] \cos(n\theta) \\
&+ \sum_{n=2,3,..}^{N} \Big[a_n' n(n-1) r^{n-2} + b_n' n(n+1) r^{n} \\
&\qquad - c_n' n(n+1) r^{-(n+2)} - d_n' n(n-1) r^{-n} \Big] \sin(n\theta)
\end{aligned} \tag{6c}
$$

The Cartesian stresses components can be evaluated from the polar stresses using the standard transformation matrix,

$$
\begin{Bmatrix} \sigma_{xx} \\ \sigma_{yy} \\ \sigma_{xy} \end{Bmatrix} = \begin{bmatrix} \cos^2\theta & \sin^2\theta & -2\sin\theta\cos\theta \\ \sin^2\theta & \cos^2\theta & 2\sin\theta\cos\theta \\ \sin\theta\cos\theta & -\sin\theta\cos\theta & \cos^2\theta - \sin^2\theta \end{bmatrix} \begin{Bmatrix} \sigma_{rr} \\ \sigma_{\theta\theta} \\ \sigma_{r\theta} \end{Bmatrix} \tag{7}
$$

Upon using Hooke's law for stress–strain relations, Eq. (1c), and the polar strain–displacement relations, one can obtain the radial and circumferential displacements, and hence, the Cartesian displacements. Determination of individual stresses, strains, or displacements necessitates evaluating the unknown Airy coefficients. Since the stress expressions of Eq. (6) does not contain the coefficients a_0, a_1 and a_1' in Eq. (4) due to the differentiation in Eq. (5), therefore there are $k = 17 + 8(N-1)$ Airy coefficients to be determined for a given summation terminal index N.

2.2.2. Additional comments on Airy coefficients

The form of the Airy stress function in Eq. (4) depends on the loading and boundary conditions, loading and geometrical symmetry, self-equilibrated at individual boundaries, single-valued stresses, strains and displacements, boundness values at origin or infinity, and whether the considered structure is infinite or finite in size. If the coordinate system is within the body structure, the single-valueless of stresses and displacements require the constants $d_0, B_0, C_0, D_0, B_1, B_1'$ to be set zero and $b_1 = (1-\nu)A_1'/2$ and $b_1' = -(1-\nu)A_1/2$ where ν is the Poisson's ratio. The four latter coefficients are zero if the considered structure is multi-connected, hence the individual boundaries are in equilibrium and no resultant forces at the origin. In a simply-connected region, these terms are single-valued if the coordinate is placed outside the body or on its boundary. If the structure has loading and geometrical symmetry about the horizontal x-axis, then the stress function is an odd function and should not contain sine terms (A_0, c_1, d_1, a_n, b_n, c_n, and d_n are all vanished). If the symmetry holds along the x- and y-axes, then only the even terms in the series expansion are retained, i.e., n is even. If the coordinate origin is within the structure (boundedness at origin) or the structure is infinite in size (boundedness at infinity), then the coefficients to prevent singularities of stresses and displacements when the radial coordinates, r, approaches zero or infinity, respectively, must be equated to zero. It is often possible to significantly reduce the number of retained Airy coefficients by satisfying some of the boundary conditions analytically [57].

3. Hybrid-ASF method

The classical plane problem of elasticity involves determining the Airy coefficients in the expressions of the stresses, Eq. (6) (and hence the strains and displacements) using the boundary conditions defined in $\partial\Omega$, Eq. (2). Unlike the classical approach, these Airy coefficients are numerically determined in a least-squares sense from possessing measured data in the from of displacements, strains, or stresses with their corresponding analytical form. The experimental data can be originated from a region R^* that is within the structure domain, i.e., $R^* \subseteq \Omega$. The distant loading and/or boundary conditions are not necessary to be well-defined in order to evaluate the Airy coefficients which render the possibility of analyzing real-life engineering applications in their operating condition. Once the Airy coefficients are evaluated from the processed data, the hybrid full-field stresses in the whole domain of the structure, Ω, can be determined from Eq. (6). The measured information on and near the edges are usually unreliable and hence can be disregarded, and only the interior data is processed into the hybrid-ASF method to predict the full-field as well as the boundary stresses. Although the general concepts of the hybrid-ASF method are applicable to multiple cutouts, arbitrarily-shaped boundaries, complicated internal discontinuities, complex loading conditions, and various processed experimental data, the current paper stress-analyze a loaded aluminum plate with a deep U-notch using TSA and the full form of ASF, Eq. (4).

3.1. Separation of stresses from load-induced measurements

Experimental techniques such as TSA and PSA provide recorded data of a loaded structure as a function of the in-plane stresses. Therefore, it is necessary to separate the individual stresses from the recorded data. For instance, the recorded surface temperatures of a cyclically-loaded isotropic structure under adiabatic condition is linearly proportional to the changes in the isopachic stress (the sum of the normal stresses), $S = \sigma_{xx} + \sigma_{yy} = \sigma_{rr} + \sigma_{\theta\theta}$. From Eq. (6), S can be written as

$$
\begin{aligned}
S &= 4c_0 + 4d_0(\ln r + 1) + 4C_0\theta + 4D_0(\ln r + 1)\theta + \left(\frac{2b_1}{r} + 8rd_1\right)\sin\theta \\
&+ \left(\frac{2b_1'}{r} + 8rd_1'\right)\cos\theta \\
&+ \frac{2A_1}{r}\cos\theta + \frac{2B_1}{r}(\theta\sin\theta + \ln r\cos\theta) - \frac{2A_1'}{r}\sin\theta \\
&+ \frac{2B_1'}{r}(\theta\cos\theta - \ln r\sin\theta) \\
&+ 4\sum_{n=2,3,..}^{\infty}\Big[b_n(n+1)r^n - d_n(n-1)r^{-n}\Big]\sin(n\theta) \\
&+ \Big[b_n'(n+1)r^n - d_n'(n-1)r^{-n}\Big]\cos(n\theta)
\end{aligned} \tag{8}
$$

Notice that S is a function of (c_0, d_0, C_0, D_0, b_1, d_1, b_1', d_1', A_1, B_1, A_1', B_1', b_n, d_n, b_n', d_n') whereas the individual stresses are functions of the same coefficients in S in addition to (b_0, A_0, B_0, c_1, c_1', a_n, c_n, a_n', c_n'). As a result, it is not sufficient to use only the isopachic stress to evaluate all the Airy coefficients. Therefore, some of the known boundary conditions should be analytically or discretely imposed in order to evaluate all the unknown coefficients.

Suppose that the m values of the isopachic stress data are known at arbitrarily locations within the region of interest R^* and there are additional h known tractions, Eq. (2a), and/or displacements, Eq. (2b), boundary conditions, a linear system of simultaneous equations can be constructed,

$$
\mathbf{A}\mathbf{c} = \mathbf{d}^* \tag{9}
$$

where the matrix $\mathbf{A} \in \mathbb{R}^{(m+h)\times k}$ consists of the analytical expressions of the m isopachic stress S, Eq. (8), and the h known stresses and/or displacements, $\mathbf{c} \in \mathbb{R}^{k\times 1}$ is the vector containing the unknown Airy coefficients, and $\mathbf{d}^* \in \mathbb{R}^{(m+h)\times 1}$ is the vector containing the corresponding values of the known m isopachic stresses in addition to the h boundary conditions. To overcome the noise incorporated with the experimental data, it is necessary to process $m + h$ measured input data that are larger than the number of the retained unknown Airy coefficients, k, i.e., $(m + h) \gg k$. The resultant overdetermined system is solved in a least-squares numerical sense in order to provide the optimum solution of the k Airy coefficients,

$$
\mathbf{c} = \left(\mathbf{A}^T\mathbf{A}\right)^{-1}\mathbf{A}^T\mathbf{d}^* \tag{10}
$$

Once $\mathbf{c}$ is determined, the counterpart of the processed data, $\mathbf{d}^*$, can be evaluated as $\mathbf{d}_{\text{Airy}} = \mathbf{A}\mathbf{c}$. The appropriate number of retained Airy coefficients is chosen based on minimizing the difference between the processed data, $\mathbf{d}^*$, and its counterpart predictions, $\mathbf{d}_{\text{Airy}}$, i.e., $\|\mathbf{d}^* -$

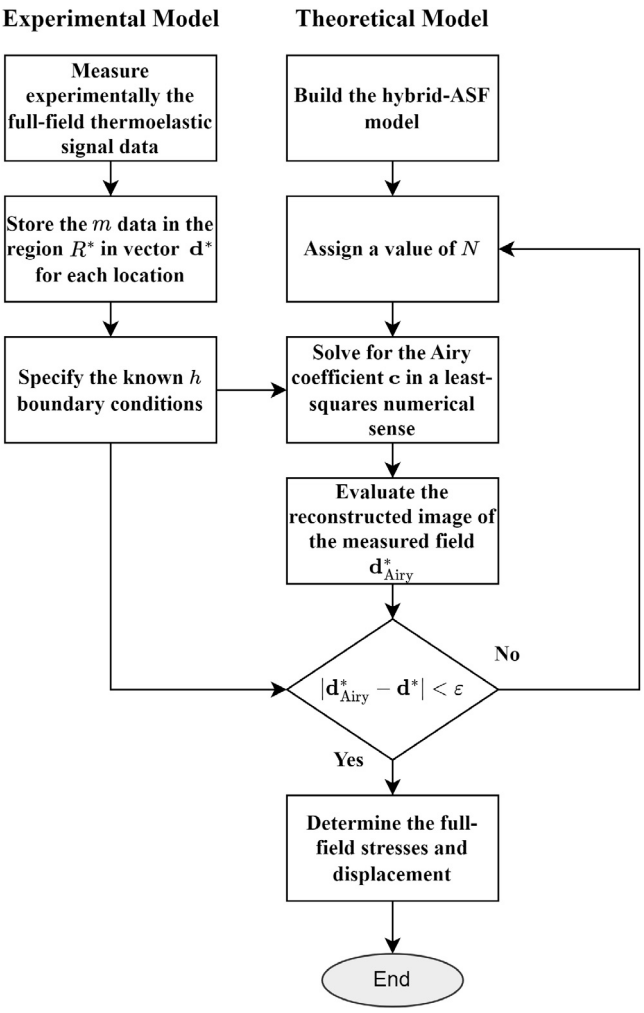

Fig. 2. Flowchart of the hybrid-ASF method for stresses separation when processing isopachic stress data.

$\mathbf{d}_{\text{Airy}}\|$. Once determining the Airy coefficients, the stresses can be determined from Eq. (6) throughout the structure domain Ω as

$$\boldsymbol{\sigma}_{rr} = \boldsymbol{\Sigma}_{rr}\mathbf{c} \qquad \boldsymbol{\sigma}_{\theta\theta} = \boldsymbol{\Sigma}_{\theta\theta}\mathbf{c} \qquad \boldsymbol{\sigma}_{r\theta} = \boldsymbol{\Sigma}_{r\theta}\mathbf{c} \tag{11}$$

where $\boldsymbol{\sigma}_{rr}, \boldsymbol{\sigma}_{\theta\theta}$, and $\boldsymbol{\sigma}_{r\theta}$ are column vector containing the corresponding values of the in-plane stresses $\sigma_{rr}, \sigma_{r\theta}$ and $\sigma_{r\theta}$ and $\boldsymbol{\Sigma}_{rr}, \boldsymbol{\Sigma}_{\theta\theta}$, and $\boldsymbol{\Sigma}_{r\theta}$ are real and rectangular coefficients matrices that are functions of the spatial locations (r, θ) and defined from Eq. (6). A flowchart for the determination of the hybrid-stresses using Airy stress function and isopachic stress data is depicted in Fig. 2.

It is worth mentioning that the hybrid-ASF method depends on: (1) the amount of the processed data, m, in the region of interest, R^*, and their locations, (2) the additional h imposed boundary conditions, (3) the terminal index, N, in the Airy stress expressions, and (4) the accuracy of the processed data. The effects of these parameters on the accuracy of the determined full-field stresses will be outlined in the subsequent sections.

4. Deep U-notched plate

4.1. Material and geometry

The in-plane stresses of a loaded finite-width aluminum plate with a deep U-notch as shown in Fig. 3 are determined from hybridizing the isopachic stress (from thermoelastic signals) with the ASF. The $2L = 5\,\text{mm}$ thick, 86 mm wide and 125 mm long plate has $2R = 2\,\text{mm}$ wide and 67 mm deep U-notch. The plate is subjected to a concentrated tensile load of $F = 356\,\text{N}$, and the coordinate's origin is at the center of the circular part of the U-notch. Since the origin is located outside the structure boundary (the periodicity of the solution in terms of θ is not applied) and the domain size is finite, all terms of the ASF were retained, Eq. (4).

The full form of the Airy stress function and the loading and geometrical symmetric along the horizontal x-axis require the enforcement of zero shear stress along the horizontal line of symmetry, $y = 0$. Therefore, the boundary conditions in terms of stresses as shown in Fig. 4 are written as

$$\sigma_{rr}(R,\theta) = \sigma_{r\theta}(R,\theta) = 0, \qquad \text{for} \quad \pi/2 \le \theta \le \pi \tag{12a}$$

$$\sigma_{yy}(x,R) = \sigma_{xy}(x,R) = 0, \qquad \text{for} \quad 0 \le x/R \le 66 \tag{12b}$$

$$\sigma_{xx}(-20R,y) = \sigma_{xy}(-20R,y) = 0, \qquad \text{for} \quad 0 \le y/R \le 20 \tag{12c}$$

$$\sigma_{xx}(66R,y) = \sigma_{xy}(66R,y) = 0, \qquad \text{for} \quad 1 \le y/R \le 20 \tag{12d}$$

$$\sigma_{xy}(x,0) = 0, \qquad \text{for} \quad -20 \le x/R \le -1 \tag{12e}$$

where R is the radius of the notch. These conditions can be imposed discretely (point-wise) at multiple locations on the traction-free boundaries of the U-notch's edge and the two outer (left and right) vertical edges of the plate.

4.2. Three-Dimensional finite-element model

For a comparison with the hybrid-TSA results and conducting an experimental numerical simulation to assess the performance and the applicability of the proposed hybrid-ASF method, a finite element analysis (FEA) using Ansys Mechanical APDL package was prepared for the finite plate of Fig. 3. The elastic properties are $E = 70\,\text{GPa}$ and $\nu = 0.33$. Due to the symmetry, only the upper half part of the plate was modeled with symmetrical boundary condition along the areas $y = 0$ and $z = 0$, Fig. 5. The eight-node solid linear elements (Solid185) were employed, and the FE model was divided into 25 planar layers across the plate thickness, i.e., the distance between two successive planes is 0.1 mm. For each plane layer, the FE model was divided into six different areas. For the area $x/R < 0$ and $y/R < 20$ that contains the circular notch, mapped meshing was utilized such that the boundary of the notch tip was discretized into 100 segments, i.e., element size $\approx$ 0.0157 mm, and the radial and transverse lines were discretized into 76 segments, i.e., element size = 0.25 mm. The rest of the five areas were meshed accordingly such that the changes in the maximum stress of the mid-plane, $z/L = 0$, between two successive meshing is less than 2%. The employed FE-model utilizes 691,625 elements and 729,092 nodes, Fig. 5.

4.2.1. Mid-plane and surface stresses

The variations of the numerically-predicted vertical stress, σ_{yy}, along the lines of symmetry for different depths z/L and along the thickness for different values of x/R are depicted in Fig. 6. It is clear that there is a difference between the predicted stresses on the surface $(z/L = 1)$ and the middle $(z/L = 0)$ planes at $x/R = -1$. This behavior agrees with the findings in [36,61,73] such that the difference between the mid-plane and surface stresses increases with the increasing of the plate's thickness. These differences become negligible when $x/R < -4.0$.

The full-field in-plane stresses on the middle and surface planes are shown in Fig. 7. For purpose of visualization, the in-plane stresses on the both planes were plotted together where the upper part corresponds to the mid-plane stresses and the lower part corresponds to the surface stresses. The xy-plane stresses throughout the plate's thickness are uniform except in the vicinity of the notch's tip. As will be shown later when employing measured surface temperatures beyond the traction-free edges, the processing of the experimental data into the solution of the ASF enables the determination of the plane stresses.

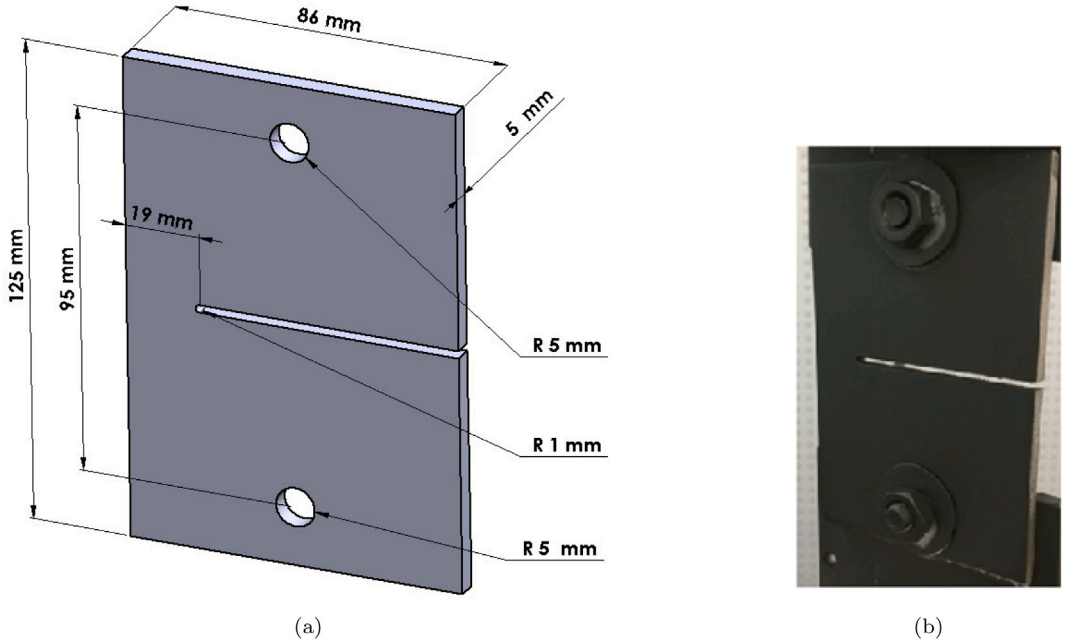

Fig. 3. (a) Plate geometry and dimensions and (b) the specimen with black paint for thermoelastic stress analysis.

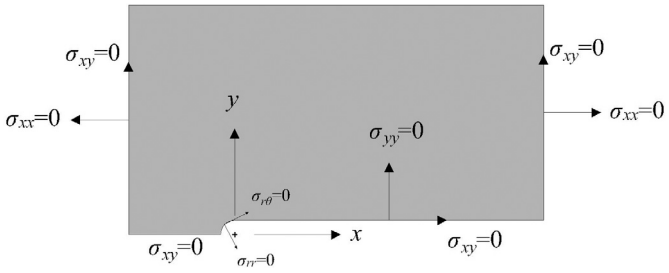

Fig. 4. Traction-free boundary conditions.

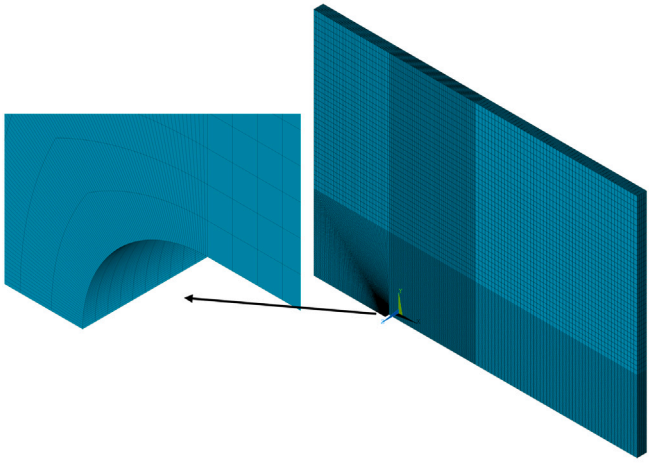

Fig. 5. Meshed FEM with dense meshing adjacent to the U-notch.

4.3. Simulated isopachic stress data

FEA was used to obtain the m in-plane isopachic stresses, S_{FE}. Standard Gaussian function $\mathcal{N}$ with a zero mean and γ standard deviation was used to simulate the superimposed noise scatter. The processed isopachic data, S, in the hybrid-ASF were deteriorated using artificial noise scatters such that $S = S_{\text{FE}} + \mathcal{N}(0,\gamma)S_{\text{FE}}$. The data were randomly originated from a region R^* that is 2 mm away from the U-notch boundary and the left and right vertical edges. The reason of not processing boundary data in the hybrid-ASF method is to demonstrate its capability in determining the boundary stresses using only the interior isopachic data. Traction-free boundary conditions along each of the free-edges were imposed at $0.1m$ discrete points, Eq. (12). Once the unknown Airy coefficients are determined from Eq. (10) using the m noisy-processed data and $h = 9 \times 0.1m$ traction-free boundary conditions, the in-plane stresses throughout the plate are obtained from Eq. (11). The hybrid-evaluated stresses are then compared with their counterparts from the FE predicted stresses. The following quantity was used to measure the difference between the hybrid-evaluated and FE-predicted stresses,

$$\Psi = \frac{\|\boldsymbol{\sigma}^{\text{FE}}_{\alpha\beta} - \boldsymbol{\sigma}^{\text{hybrid}}_{\alpha\beta}\|}{\|\boldsymbol{\sigma}^{\text{FE}}_{\alpha\beta}\|} \times 100, \qquad \alpha,\beta = x,y \text{ or } r,\theta \tag{13}$$

where $\|\cdot\|$ is the second norm. The purpose of the numerical experiment is to assess the effects of the terminal index, N, in the ASF, the noise level quantified by γ, the amount and location of the processed data in separating the full-field stresses from isopachic stress.

4.3.1. Number of retained terms in ASF

The number of series terms, N, in ASF of Eq. (4) was selected based on minimizing the norm difference between the m processed noisy data with $\gamma = 10\%$ and $0.9m$ traction-free conditions, vector $\mathbf{d}^*$, with their predicted counterpart, $\mathbf{Ac}$, from the hybrid method, i.e., $\|\mathbf{Ac} - \mathbf{d}^*\|$, as shown in Fig. 8(a). Upon retaining additional terms in ASF where $k = 17 + 8(N-1)$ and $N \geq 2$, the difference between the predicted, $\mathbf{Ac}$, and processed, $\mathbf{d}^*$, data is decreased until the matrix coefficient, $\mathbf{A}$, becomes unstable, due to its large condition number. The minimum number of Airy coefficients to retain depends on the number of processed data, m. For instance, processing $m = 250$ isopachic data necessitate retaining at most $k = 57$ ($N = 6$) coefficients comparing when processing $m \geq 1000$ data which require retaining at most $k = 49$ ($N = 5$) coefficients in the ASF. Even though only the interior isopachic stress data were processed, the hybrid-ASF method was able to separate the isopachic stress into the individual stress components. The hybrid-evaluated stress components throughout the plate (including the boundary where no information were processed) are compared

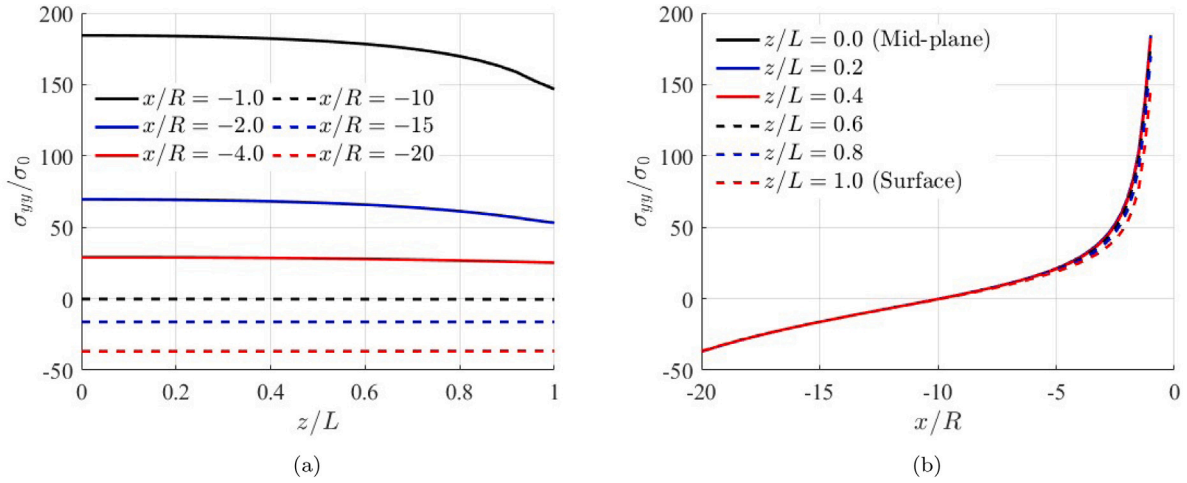

Fig. 6. Numerically-predicted vertical stress, σ_{yy}, at $y = 0$ and (a) along the lines of symmetry x/R for different depths z/L and (b) through the thickness z/L for different values of x/R.

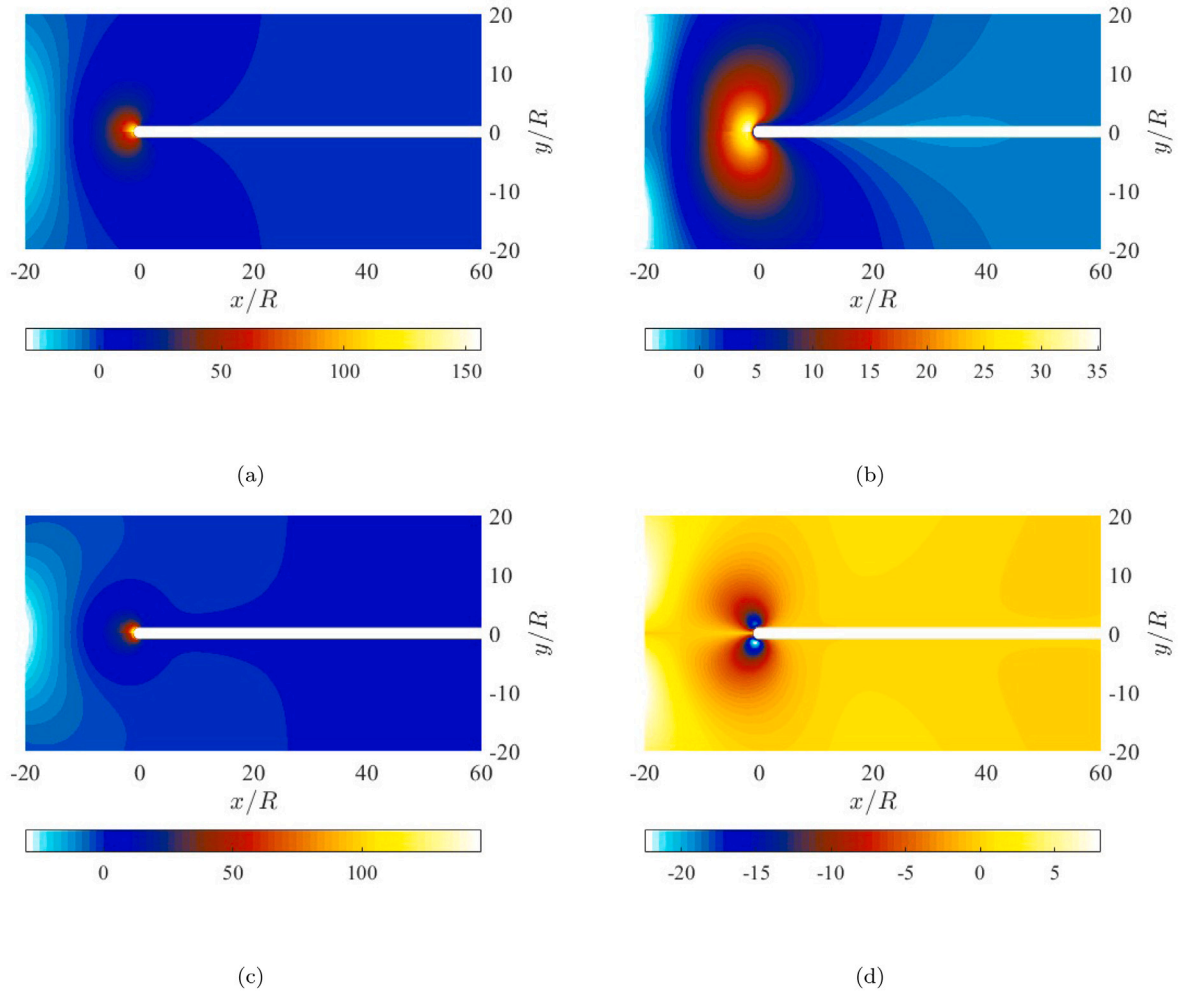

Fig. 7. Contour plots of (a) isopachic stress $S = \sigma_{xx} + \sigma_{yy}$, (b) σ_{xx}, (c) σ_{yy}, and (d) σ_{xy} in (MPa) on the middle (upper) and surface (lower) planes.

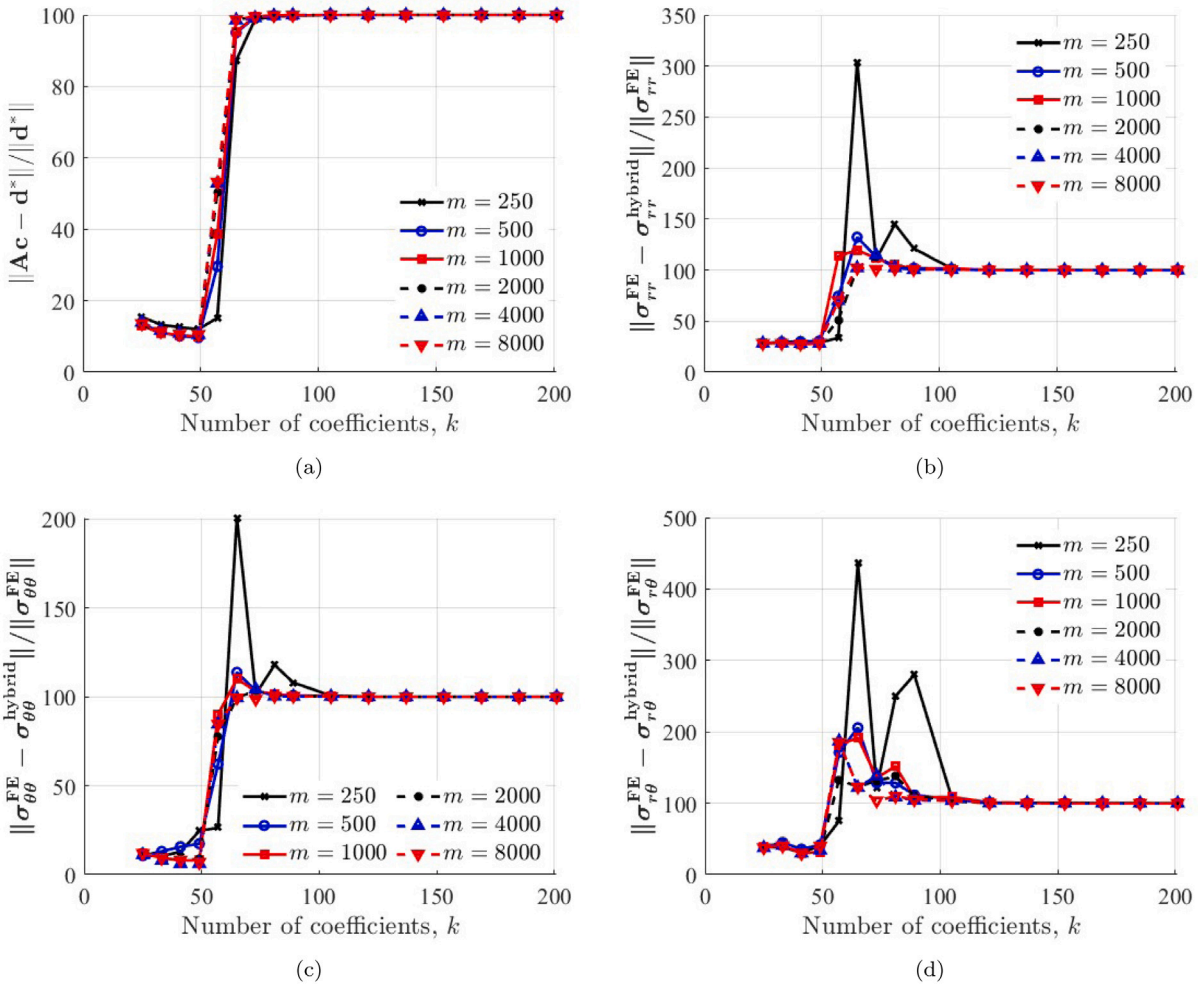

Fig. 8. The variation of the norm difference between the (a) processed data d^*, (b) radial stress σ_{rr}, (c) tangential stress $\sigma_{\theta\theta}$, and (d) shear stress $\sigma_{r\theta}$ from the hybrid-ASF method with FE-predictions when using different number of retained coefficients, N, $\gamma = 10\%$ and different number of randomly-located processed data, m, in the region R^*.

with the FE-predicted stresses as shown in Figs. 8(b) to 8(d). Even though the processed data were artificially deteriorated, the hybrid-evaluated stress are 20% within the FE-predicted stresses. Therefore, Fig. 8 suggests of selecting an appropriate number of retaining coefficients in ASF, Eq. (4), that simultaneously stabilize the coefficient matrix **A**, and minimize the difference between the processed data and its counterpart evaluated in a least-squares sense.

4.3.2. Assessing the effects of the number of employed data

From the previous analysis, it is appropriate to retain $k = 49$ ($N = 5$) coefficients in the ASF of Eq. (4). The variation of the norm difference between the hybrid-evaluated and FE-predicted stresses with the number of employed data, m, for different noise levels, γ, are illustrated in Fig. 9. It worth to mention that each data point in Fig. 9 represents the average of 10 different sets of m randomly-located data in the region R^*. It is clear from Fig. 9(a) that the hybrid-ASF filters out the artificially added noise in the processed data. The larger the noise level added to deteriorate the processed data, the larger the difference between the processed, $\mathbf{d}^*$, and the re-constructed, $\mathbf{Ac}$, vectors is. This can be supported by the consistency of the hybrid-evaluated stresses for a large set of employed data $m > 2000$ regardless of the added noise levels in the processed data. For a set of $m \leq 2000$ data points, adding artificial noise/scatter into the processed data deteriorates the accuracy of the obtained hybrid-stresses. The evaluated tangential stress correlates very well with the FE-predicted stresses (within 10%) compared to the radial (within 30%) and shear (within 35%) stresses, Figs. 9(c) vs. 9(b) and 9(d). This is because of the larger magnitudes of the former comparing to the latters. Hence, it is necessary to employ larger data set when processing actual experimental information in order to obtain accurate and precise hybrid-stresses.

4.3.3. Assessing the effects of the added noise level in the processed data

Fig. 10 shows the norm difference between the hybrid-evaluated and FE-predicted stresses with the artificial added noise level, γ, for different number of employed data, m. The hybrid-ASF does filter out the artificially added noise into the processed data, Fig. 10(a), but do not guarantee the accuracy of the determined hybrid stresses, Figs. 10(b) to 10(d), for noisy deteriorated data. The larger the employed data set is, the accurate the hybrid-evaluated stresses are. For instance, the evaluated stresses start to deviate from the FE-predicted stresses for $m \leq 1000$ employed data at the noise level of $\gamma = 20\%$. However, for a data set of $m \geq 2000$, the evaluated stresses at the noise level of $\gamma = 40\%$ start to deviate from the FE-predicted stresses. Beyond the noise level of $\gamma > 50\%$, the hybrid-ASF starts to fail in predicting accurate stresses.

4.4. Thermoelastic Stress Analysis (TSA)

Experimental TSA technique provides the full-field thermal stresses of actual loaded structures that are operated in their working environment. Since the induced loading information is related to the

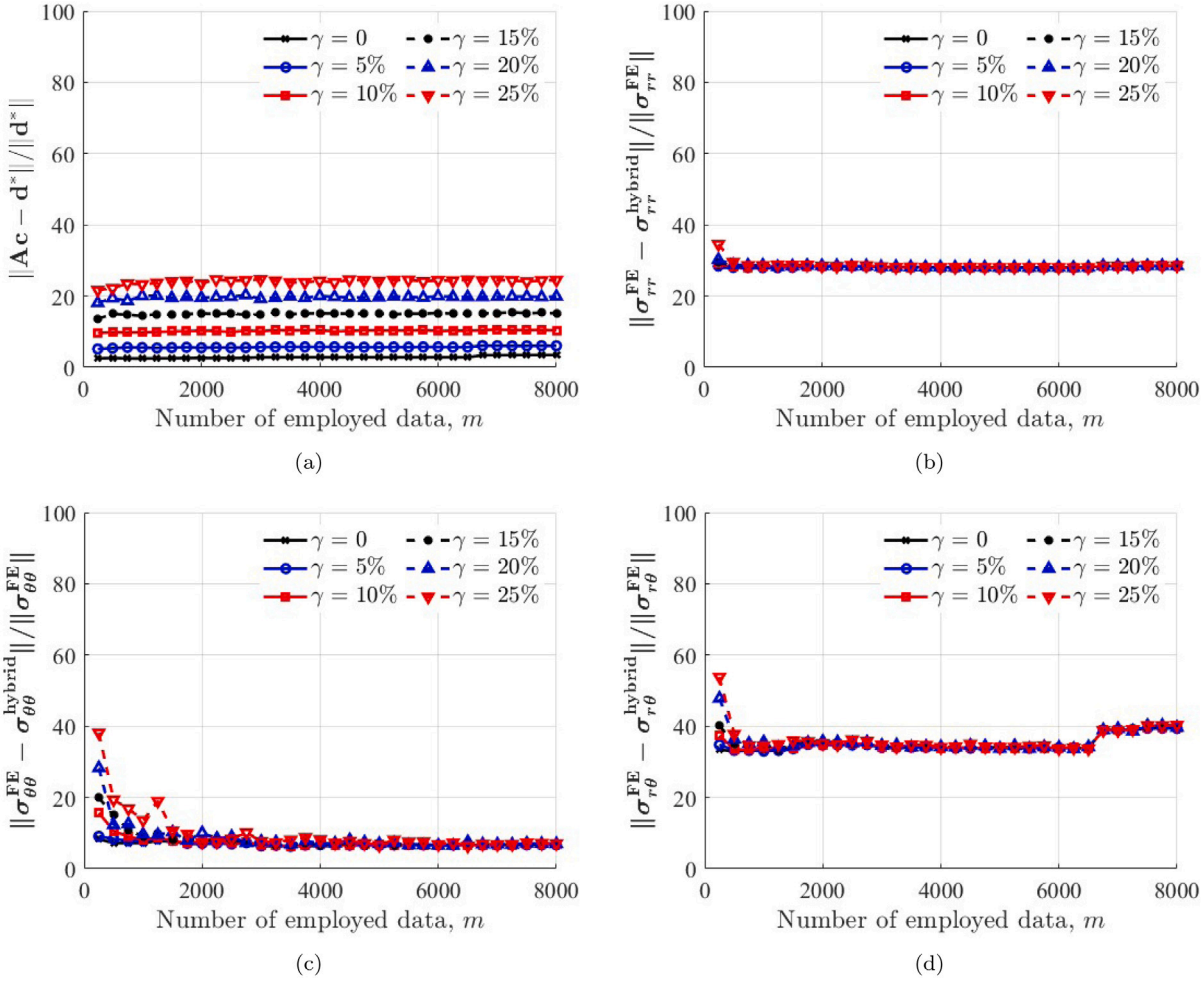

Fig. 9. The variation of the norm difference between the (a) processed data d^*, (b) radial stress σ_{rr}, (c) tangential stress $\sigma_{\theta\theta}$, and (d) shear stress $\sigma_{r\theta}$ from the hybrid-ASF method with FE-predictions when using different number of employed data, m, in the region R^* and different values of noise levels, γ.

temperature changes (also known as TSA signals), sensitive infrared camera is usually used to record such thermal information. TSA has a sensitivity that is comparable with the strain gauges. The isotropic structure has to be cyclically loaded to satisfy adiabatic and reversible conditions in order to linearly relate the isopachic stresses, S, to the load-induced TSA thermal information, S^*, at a certain location, i.e., $S^* = KS$, where K is a TSA calibration factor (thermoelastic material coefficient). This coefficient which depends on the used TSA system parameters, the surface conditions of the loaded structure, and the physical properties of the material is determined experimentally [74]. From thermodynamic reasons, the induced cyclic loading provides unreliable recorded TSA data at the edges (pixels can straddle the boundary).

4.4.1. Experimental setup and data processing

The specimen of Fig. 3 was initially polished with 400 grit sand paper and then painted with a coating of Krylon Ultra-Flat black paint to enhance and uniform its emissivity. Precaution was taken when sanding the faces of the specimen not to round-off the edges in the proximity of the U-notch which could affect the quality of the recorded thermal information. The plate was sinusoidally loaded in a 20 kips capacity MTS hydraulic testing machine with a mean load of $F_m = 1068$ N, a load range of $\Delta F = 356$ N, and a frequency of 30 Hz, Fig. 11. Hence, the load ratio is 0.7143. The corresponding load-induced information, S^*, were recorded using a Delta Therm Stress Photonics TSA system software (model DT1410) which have a sensor array of 256 × 256 pixels. To have accurate thermal information readings, a liquid nitrogen is used to cool down the system in order to maintain the sensor at a very low temperature. The camera was aligned perpendicular to the surface of the plate, Fig. 11(a). The plate was loaded at different cyclic rates while monitoring the phase information provided in order to ensure the adiabatic conditions are prevailed at the employed loading frequency. TSA images were captured and averaged over two minute duration, and then converted each pixel (of size 0.35 mm) into a data point, i.e., 256 by 256 matrix. The thermoelastic coefficient K was evaluated from a separate uniaxial tensile coupon of the same material, thickness and flat black paint coating, and the coupon was tested on the same day, frequency and TSA arrangement as the U-notched plate. The thermoelastic coefficient was determined to be $K = 212$ U/MPa. The unit [U] is used to signify the raw TSA output, in uncalibrated signal units. Detailed experimental information regarding data acquisition, processing, and analyzing can be found in [75].

Since the plate geometry and loading are symmetrical about the horizontal x-axis, the upper and lower recorded thermoelastic data, S^*, of Fig. 11(b) were first averaged. Recognizing the unreliability of the TSA data on and near edges, no recorded TSA information was used within at least three to six pixels positions (1.1 to 2.1 mm) of the boundary, Fig. 12. Only the $m = 10{,}461$ thermal values of S^* originated at the locations shown in Fig. 13 were processed with the ASF. Like most experimental data, the recorded S^* includes some noise which

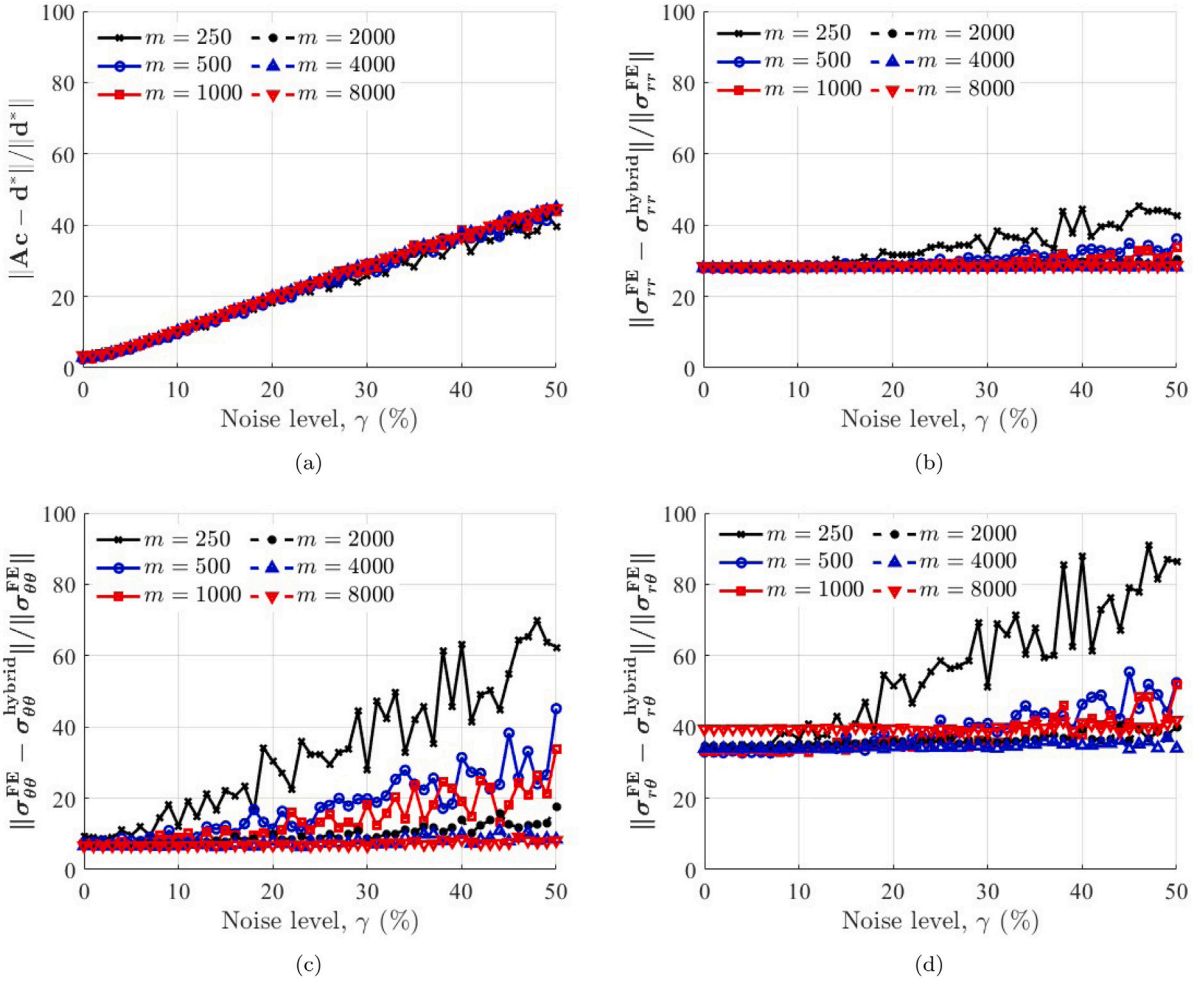

Fig. 10. The variation of the norm difference between the (a) processed data d^*, (b) radial stress σ_{rr}, (c) tangential stress $\sigma_{\theta\theta}$, and (d) shear stress $\sigma_{r\theta}$ from the hybrid-ASF method with FE-predictions when using different values of superimposed noise levels, γ and different number of employed data, m, in the region R^*.

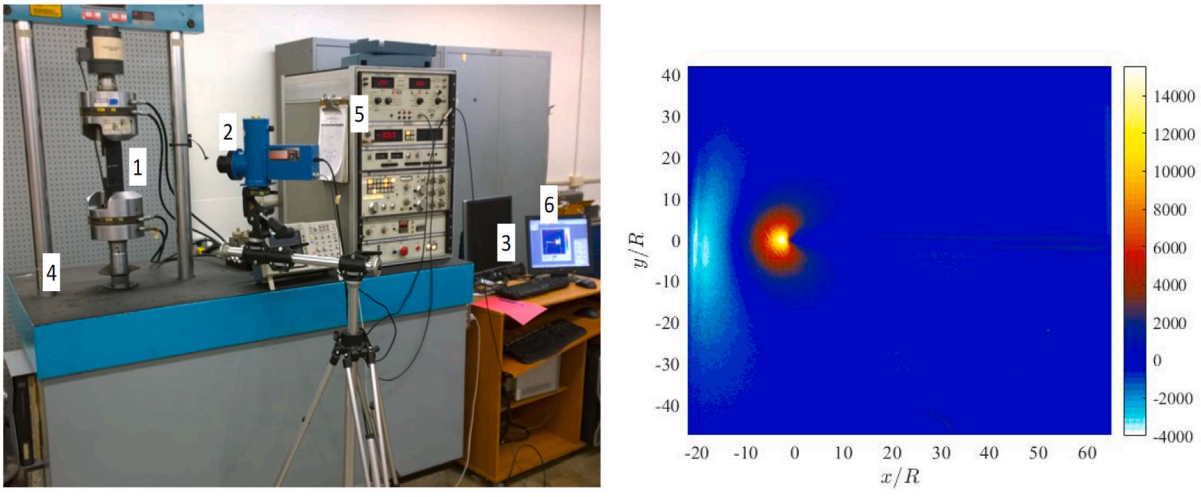

Fig. 11. (a) Experimental test setup for recording temperature variations of (1) finite plate with U-notch using (2) Delta Therm model DT1410 infrared camera, (3) computer to analyze the recorded image data, (4) the loading frame of the MTS testing machine, (5) the control panel of the servo-hydraulic testing machine, and (6) TSA image of loaded specimen and (b) TSA image with load range of 356 N and frequency 30 Hz.

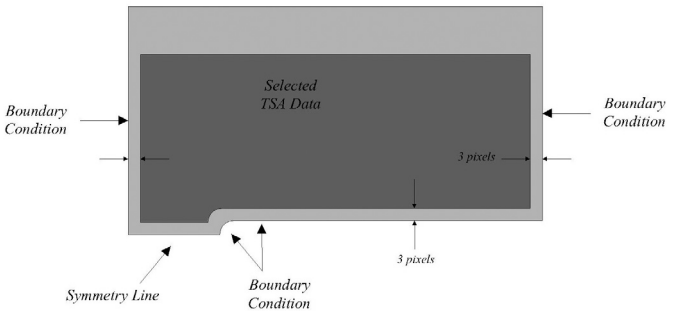

Fig. 12. Source locations of the selected TSA data and the locations of the imposed boundary conditions and the line of symmetry.

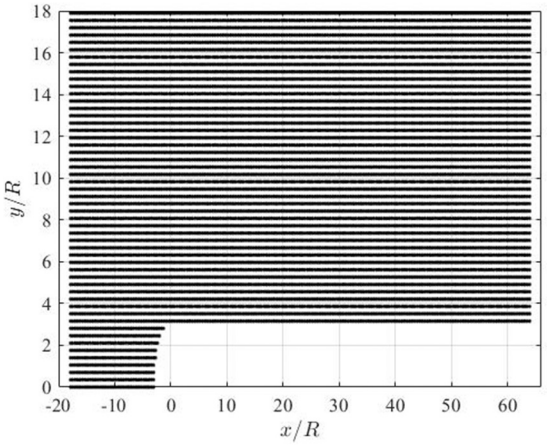

Fig. 13. Source locations of employed S^* data (m = 10,461 data points).

necessitates collecting more measured input values than the number of unknown coefficients. Furthermore, $h = 500 \times 9 = 4500$ boundary conditions were imposed at 500 equally-spaced discrete points on each of the nine relevant expressions in Eq. (12) on the lines of Fig. 4. The number of equations, $m + h = 14961$, exceeds the number of retained Airy coefficients, k, which necessitate solving the resultant overdetermined system in least-squares sense, Eq. (10).

4.4.2. Results of hybrid stresses

The number of retained Airy coefficients was selected based on the rms difference between the processed data $\mathbf{d}^*$ and the reconstructed one, $\mathbf{d}_{\text{Airy}}$, as shown in Fig. 14(a). The $k = 49$ Airy coefficients were retained since the rms difference is increased beyond this value. The selection of this value is also supported by comparing the reconstructed image from the hybrid-ASF method with the recorded S^* data as shown in Fig. 14(b).

Fig. 15(a) shows the hybrid stresses along the line of symmetry, $-22 \le x/R \le -1$ and $y = 0$, with the FE-predictions where Figs. 15(b) through 15(d) illustrate the contour plots of the polar stresses. Even though no thermal information in the proximity of the U-notch edges were employed in the hybrid-ASF method, the obtained results from the discrete TSA input values, S^*, agree virtually with finite-element predictions throughout the specimen.

4.5. Strain gauge analysis

The present hybrid approach was further validated by comparing the obtained hybrid strains at the static load of 356 N (80 lb) with those from small commercial foil strain gauges mounted away from the boundary of the U-notch by 2.5 mm on the front surface, Fig. 16(a), and 2.0 and 2.8 mm on the back surface, Fig. 16(b). Four single-element Micro-Measurements strain gauges (EA-06-015DJ-120), each having gauge resistance of 120.0 ± 0.3% Ω and gauge factor of 2.05 ± 1.0%, were mounted along the line $y = 0$ on the specimen (two gauges on the front face and two on the back face). One of the four gauges was malfunctioned. The present gauges were mounted using standard strain gauge procedures suggested by Vishay Micro-Measurements. The recommended conditioners and neutralizers were used on the aluminum before mounting the gauges. M-Bond 610 adhesive was utilized in conjunction with a 200 Catalyst-C for good adhesion and long-time stability. A protective air drying polyurethane coating, M-Coat, was applied over the gauges and their wires after the adhesive had dried. Although the gauges were not 'tuned' for aluminum, they were mounted and the testing was conducted at room temperature so no dummy temperature compensating gauges were employed. Figs. 16(c) and 16(d) show the test arrangement for recording the strain gauge data. There photographs includes the overall testing of the deeply grooved finite plate, and associated strain gauge cables and instrumentation.

Fig. 17(a) shows the linear response of the recorded strains with the load levels of plate. All strain-gauge results were recorded under both incremental increasing and decreasing static loading. The strain gauge tests were conducted under individual loading and after removing the black paint from the TSA-tested plate. Fig. 17(b) compares the strains induced from an equivalent static load of $F = 356$ N along the line $y = 0$ obtained from hybrid-ASF method with those from FEM and strain gauges. The good agreement in Fig. 17(b) supports the reliability of the proposed hybrid method and its ability in obtaining reliable individual stresses from processing only recorded thermal information beyond the edges of internal discontinuities.

5. Conclusions

The full-field in-plane stresses of a finite plate with a deeply grooved U-notch has been determined by processing the load-induced TSA signals with ASF, together with discretely imposing some of the known boundary conditions, and without neither knowing the far-field applied loading nor using any supplemental experimental information in the form of measured isoclinics or ischromatics (from PSA) or displacements (from DIC). Even though no recorded TSA data along, and adjacent to, the deep U-notch were employed (due to unreliability or even unavailability of such information), the hybrid-ASF evaluates accurate boundary (edge) information and provides reliable full-field data, i.e., filtering out the experimental noise/scatter and smoothing the results, from only processing the interior TSA data. Although the present hybrid-ASF is applicable to stress-analyze complicated problems experimentally which cannot be analyzed numerically, the FEM was used to predict numerical results with which to validate the obtained experimental results. The reliability of the experimental hybrid results was also supported through comparison with strain gauges measurements. It is worth mentioning that the proposed hybrid-ASF method is applicable to single and multiple cutouts, loaded and free boundaries, various loading conditions, complicated internal discontinuities, complex external geometries, and various types of processed experimental data. However, since the Michell general solution of ASF was employed as the analytical ingredient of the hybrid method, it is only limited to linear elastic isotropic response.

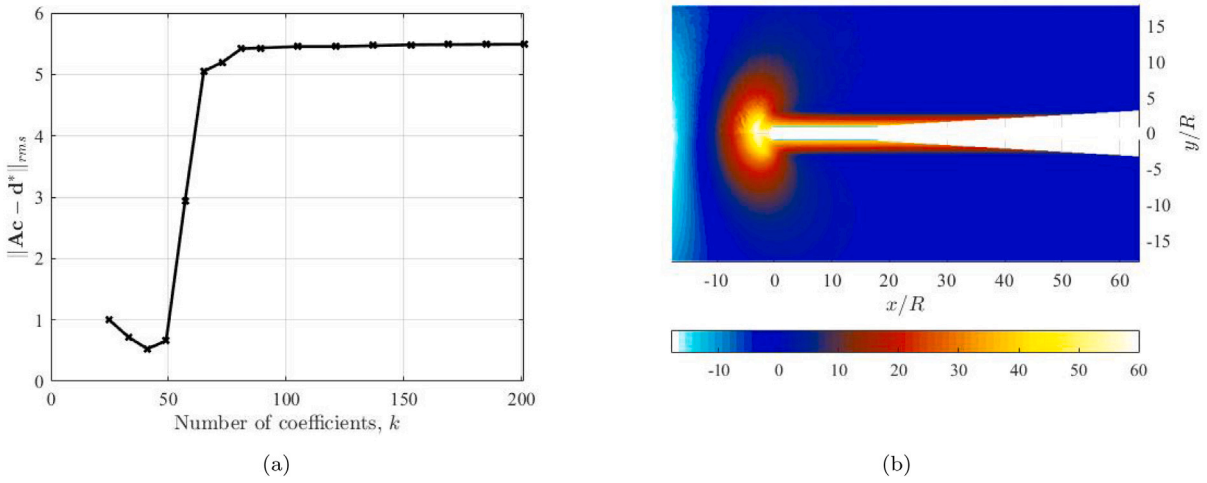

Fig. 14. (a) The rms of the difference between the processed and reconstructed thermoelastic data versus the number of retained Airy coefficients, k ($m+h$ = 14,961 data points) and (b) $S = S^*/K$ in MPa from TSA (upper) and reconstructed using ASF (lower).

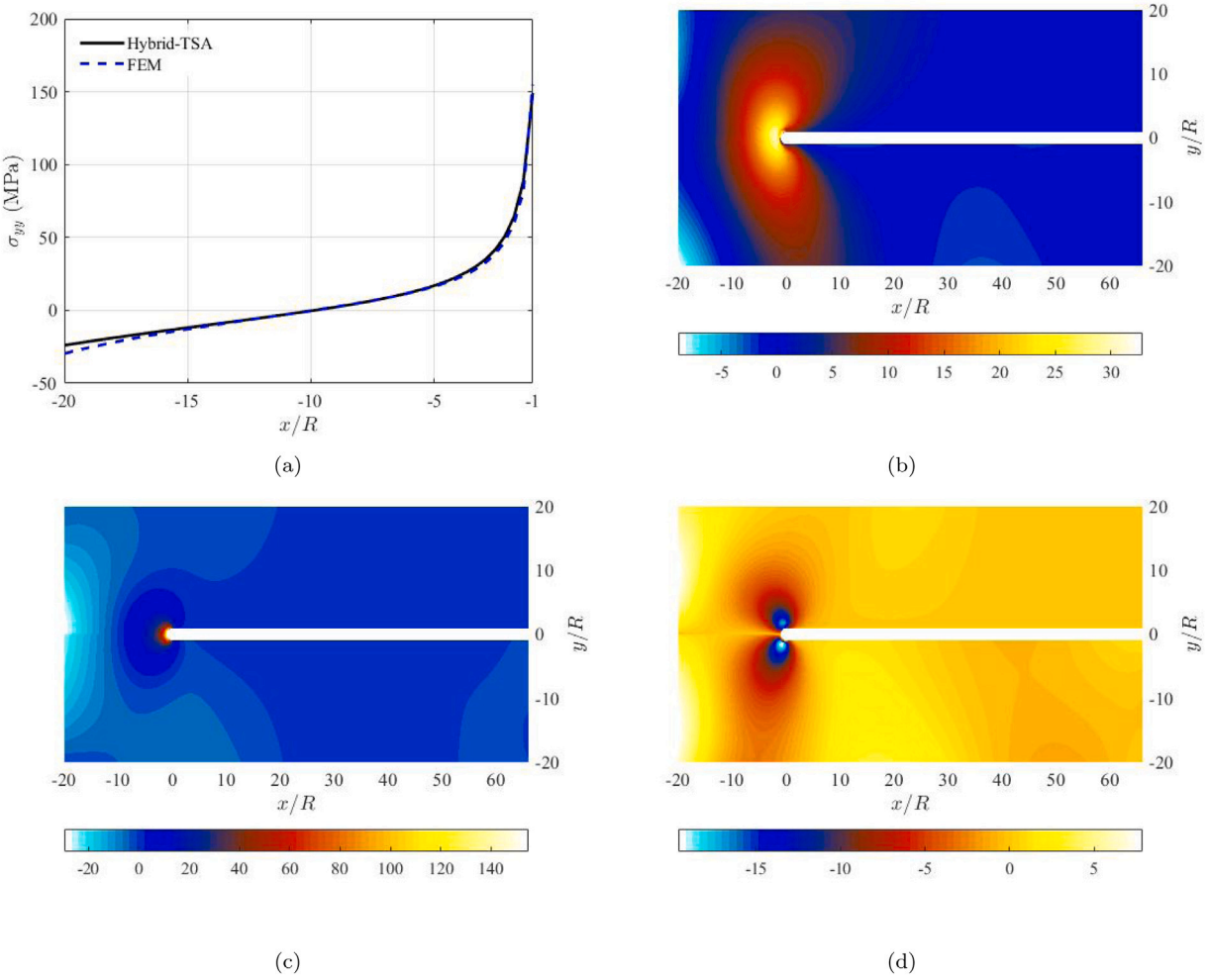

Fig. 15. (a) Variations of the normal stress σ_{yy} along the line $y = 0$ and contour plots of the polar stresses: (b) radial stress, σ_{rr}, (c) tangential stress, $\sigma_{\theta\theta}$, and (d) shear stress $\sigma_{r\theta}$ in (MPa) from FEM (upper) and hybrid method (lower) using $m+h$ = 14,961 data points and k = 49.

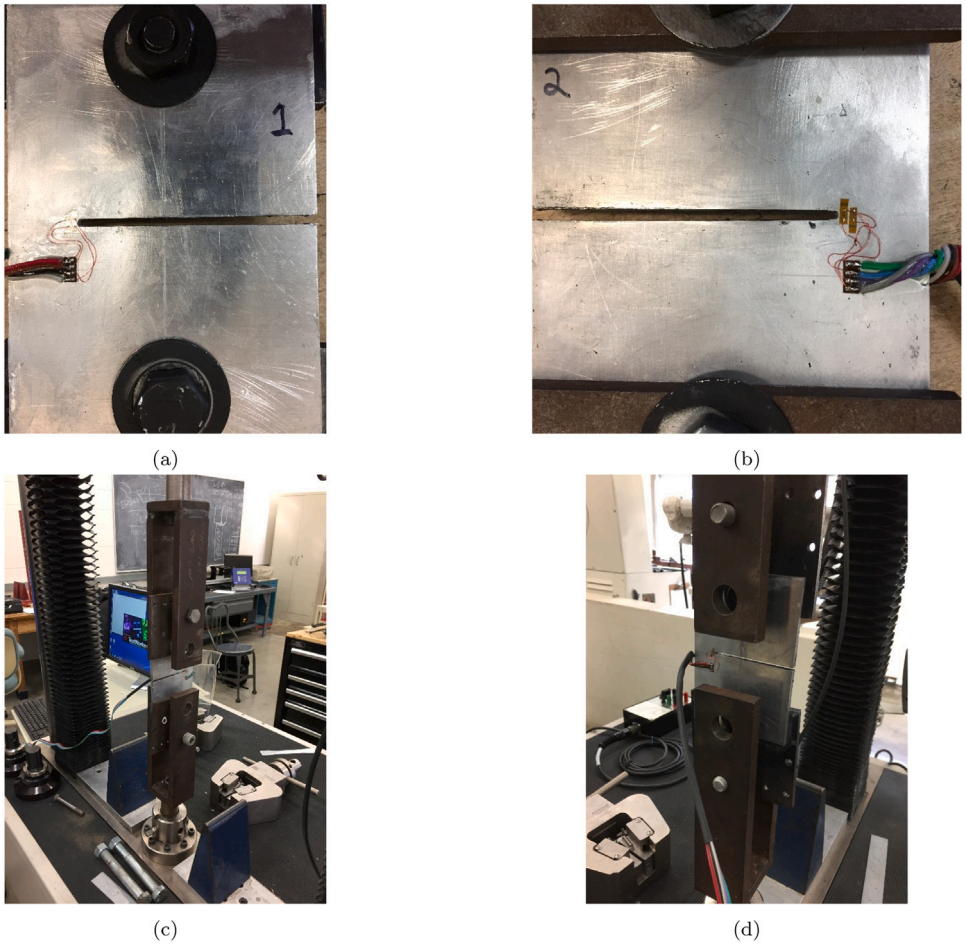

Fig. 16. Specimen's (a) front and (b) back surfaces with mounted strain gauges, and (c) and (d) the experimental testing setup for measuring the vertical strain of the deeply grooved finite plates using the strain gauges.

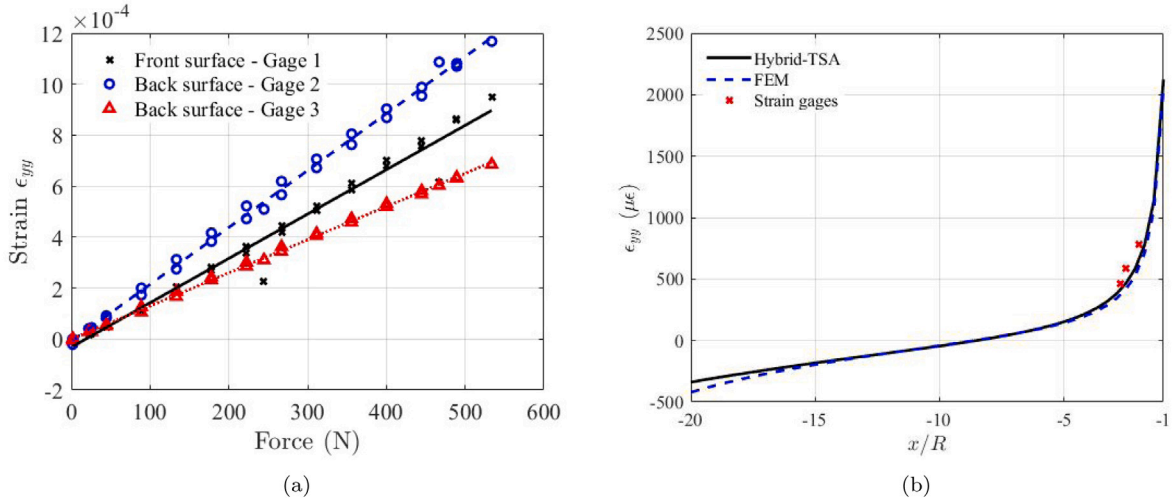

Fig. 17. (a) Recorded strains for different static loadings and (b) vertical strains ϵ_{yy} along the line $y = 0$ with a load of $\Delta F = 356\,\mathrm{N}$ from strain gauges, FEM, and hybrid method using $m + h = 14{,}961$ data points and $k = 49$.

CRediT authorship contribution statement

Abdullah A. Alshaya: Conceptualization, Methodology, Software, Validation, Formal analysis, Investigation, Writing – original draft, Writing – review & editing, Visualization.

Declaration of competing interest

The authors declare the following financial interests/personal relationships which may be considered as potential competing interests: Abdullah Alshaya reports equipment, drugs, or supplies was provided by University of Wisconsin-Madison.

Data availability

Data will be made available on request.

Acknowledgments

The author would like to acknowledge both Professor R. Rowlands at UW-Madison (Emeritus) and Professor J. L. Freire at Pontifical Catholic University of Rio de Janeiro for their valuable suggestions and comments in improving the manuscript and B. Yang, S. Krunthottikkal Philip, and J. Zeuske at UW-Madison for their contributions in conducting the TSA experiments.

Funding

This research received no specific grant from any funding agency in the public, commercial, or not-for-profit sectors.

References

[1] S.G. Lekhnitskii, Theory of elasticity of an anisotropic elastic body, first ed., Holden-Day, San Francisco, 1963.
[2] S. Timoshenko, J. Goodier, Theory of Elasticity, third ed., McGraw-Hill Publishing Company, New York, 1970.
[3] N. Muskhelishvili, Some Basic Problems of the Mathematical Theory of Elasticity, 1977 ed., Springer, Leyden, 1977.
[4] I.S. Sokolnikoff, Mathematical Theory of Elasticity, Krieger Pub Co, Malabar, Fla, 1983.
[5] R.W. Soutas-Little, Elasticity, Dover Publications, 1999.
[6] J.W. Dally, W. Riley, Experimental Stress Analysis, third sub ed., Mcgraw-Hill College, New York, 1991.
[7] A. Shukla, J. Dally, Experimental Solid Mechanics, College House Enterprise, LLC, Knoxville, 2010.
[8] C.A. Sciammarella, F.M. Sciammarella, Experimental Mechanics of Solids, first ed., Wiley, Chichester, West Sussex, U.K, 2012.
[9] G.N. Savin, Stress Concentration Around Holes, Pergamon Press, 1961.
[10] W.D. Pilkey, D.F. Pilkey, Peterson's Stress Concentration Factors, third ed., Wiley, Hoboken, N.J, 2008.
[11] R.B. Heywood, Designing By Photoelasticity, Chapman & Hall, 1952.
[12] A. Kuske, C. Robertson, Photoelastic Stress Analysis, John Wiley & Sons Ltd, London, 1974.
[13] B.J. Rauch, R.E. Rowlands, Thermoelastic Stress Analysis, second ed., in: Handbook of Experimental Mechanics, VCH Publishers, New York, 1993.
[14] K.G. McConnell, W.E. Riley, Strain-gage instrumentation and data analysis, in: Handbook on Experimental Mechanics, second rev. ed., A.S. Kobayashi, VCH, 1993, pp. 79–117.
[15] R. Greene, E. Patterson, R. Rowlands, Thermoelastic stress analysis, in: J. Sharpe, N. William (Eds.), Springer Handbook of Experimental Solid Mechanics, Springer US, 2008, pp. 743–768.
[16] E.A. Patterson, R.E. Rowlands, Determining individual stresses thermoelastically, J. Strain Anal. Eng. Des. 43 (6) (2008) 519–527.
[17] A.S. Kobayashi, Hybrid experimental-numerical stress analysis, Exp. Mech. 23 (3) (1983) 338–347.
[18] S. Atluri, T. Nishioka, Chapter 3 hybrid methods of analysis, in: North-Holland Mathematics Studies, Vol. 94, North-Holland, 1984, pp. 65–95.
[19] T. Nishioka, Hybrid numerical methods in static and dynamic fracture mechanics, Opt. Lasers Eng. 32 (3) (1999) 205–255.
[20] P. Stanley, W.K. Chan, Quantitative stress analysis by means of the thermoelastic effect, J. Strain Anal. Eng. Des. 20 (3) (1985) 129–137.
[21] P. Stanley, Appraisal of a new infrared-based stress analysis technique, Opt. Eng. 26 (1) (1987) 75–80.
[22] P. Stanley, W.K. Chan, The application of thermoelastic stress analysis techniques to composite materials, J. Strain Anal. Eng. Des. 23 (3) (1988) 137–143.
[23] P. Stanley, Applications and potential of thermoelastic stress analysis, Achiev. Mech. Mater. Eng. 64 (1) (1997) 359–370.
[24] J. Dulieu-Smith, P. Stanley, On the interpretation and significance of the grüneisen parameter in thermoelastic stress analysis, J. Mater Process. Technol. 78 (1) (1998) 75–83.
[25] J.M. Dulieu-Barton, P. Stanley, Development and applications of thermoelastic stress analysis, J. Strain Anal. Eng. Des. 33 (2) (1998) 93–104.
[26] J.M. Dulieu-Barton, Introduction to thermoelastic stress analysis, Strain 35 (2) (1999) 35–39, Publisher: John Wiley & Sons, Ltd.
[27] J. Dulieu-Barton, P. Stanley, Applications of thermoelastic stress analysis to composite materials, Strain 35 (2) (1999) 41–48.
[28] S. Lin, W. Samad, A. Khaja, R. Rowlands, Hybrid thermoelastic stress analysis, Exp. Mech. 55 (4) (2015) 653–665.
[29] A. Eremin, P. Lyubutin, S. Panin, R. Sunder, Application of digital image correlation and Williams series approximation to characterize mode I stress intensity factor, Acta Mech. (2022).
[30] J. Shuai, J. Zhao, L. Lei, Simple crack tip and stress intensity factor determination method for model I crack using digital image correlation, Theor. Appl. Fract. Mech. 122 (2022) 103621.
[31] S. Lin, Z. Feng, R. Rowlands, Thermoelastic determination of stress intensity factors in orthotropic composites using the J-integral, Eng. Fract. Mech. 56 (4) (1997) 579–592.
[32] R.A. Tomlinson, A.D. Nurse, E.A. Patterson, On determining stress intensity factors for mixed mode cracks from thermoelastic data, Fatigue Fract. Eng. Mater. Struct. 20 (2) (1997) 217–226, Publisher: John Wiley & Sons, Ltd.
[33] R.A. Tomlinson, E.J. Olden, Thermoelasticity for the analysis of crack tip stress fields — a review, Strain 35 (2) (1999) 49–55, Publisher: John Wiley & Sons, Ltd.
[34] F.A. Díaz, E.A. Patterson, R.A. Tomlinson, J.R. Yates, Measuring stress intensity factors during fatigue crack growth using thermoelasticity, Fatigue Fract. Eng. Mater. Struct. 27 (7) (2004) 571–583, Publisher: John Wiley & Sons, Ltd.
[35] T. Sakagami, Y. Izumi, N. Mori, S. Kubo, Development of self-reference lock-in thermography and its application to remote nondestructive inspection of fatigue cracks in steel bridges, Quant. InfraRed Thermogr. J. 7 (1) (2010) 73–84.
[36] R.B. Vieira, G.L.G. Gonzáles, J.L.F. Freire, Thermography applied to the study of fatigue crack propagation in polycarbonate, Exp. Mech. 58 (2) (2018) 269–282.
[37] F.I. Baratta, D.M. Neal, Stress-concentration factors in u-shaped and semi-elliptical edge notches, J. Strain Anal. 5 (2) (1970) 121–127, Publisher: SAGE Publications.
[38] S.T. Lin, R.E. Rowlands, Thermoelastic stress analysis of orthotropic composites, Exp. Mech. 35 (3) (1995) 257–265.
[39] A. Alshaya, R. Rowlands, Experimental stress analysis of a notched finite composite tensile plate, Compos. Sci. Technol. 144 (2017) 89–99.
[40] S. Zahedi, C. Kodsi, F. Berto, Numerical predictions of U-notched sample failure based on a discrete energy argument, Theor. Appl. Fract. Mech. 100 (2019) 298–306.
[41] M. Zappalorto, M. Ricotta, Effect of material orthotropy on the notch stress intensity factors of sharp V-notched plates under tension, Theor. Appl. Fract. Mech. 104 (2019) 102375.
[42] A. Torabi, B. Saboori, A. Ghelich, Fracture of U- and V-notched Al6061-T6 plates: The first examination of the fictitious material concept under mixed mode I/III loading, Theor. Appl. Fract. Mech. 109 (2020) 102766.
[43] A. Torabi, H. Talebi, M. Ayatollahi, M. Petru, Mixed mode I-III fracture resistance of stainless steel 316L weakened by V-notches with end holes, Theor. Appl. Fract. Mech. 122 (2022) 103574.
[44] M. Serati, H. Alehossein, D.J. Williams, Elastic stress analysis of partially loaded hollow discs, Internat. J. Engrg. Sci. 53 (2012) 19–37.
[45] M. Serati, D.J. Williams, Michell–Fourier analytical treatment of stresses in the ring test under parabolic compression, 2015, pp. ARMA–2015–150.
[46] M. Serati, H. Alehossein, D.J. Williams, Theoretical treatment of disc cutters subjected to general cutting forces, J. Eng. Math. 100 (1) (2016) 141–165.
[47] H. Goleij, R. Faal, A. Fotuhi, Mixed mode cracks in annular planes of cylindrical orthotropy subjected to inplane loading, Theor. Appl. Fract. Mech. 93 (2018) 1–18.
[48] G. Singh, T.K. Bhandakkar, Simplified approach to solution of mixed boundary value problems on homogeneous circular domain in elasticity, J. Appl. Mech. 86 (2) (2018) 021007–021007–9.
[49] U. Arasan, S. Venkatachalam, H. Murthy, Solution to two-dimensional elastic problems involving functionally graded material in radial co-ordinates, Acta Mech. 233 (1) (2022) 343–362.
[50] Y.S. Thube, S.K. Lohit, T.P. Gotkhindi, A coupled analytical–FE hybrid approach for elastostatics, Meccanica 55 (11) (2020) 2235–2262.
[51] B.E. Foust, R.E. Rowlands, Thermoelastic determination of individual stresses in a diametrally loaded disk, Strain 47 (2) (2011) 146–153.
[52] S.-J. Lin, D.R. Matthys, R.E. Rowlands, Separating stresses thermoelastically in a central circularly perforated plate using an airy stress function, Strain 45 (6) (2009) 516–526.
[53] A. Khaja, D. Matthys, R. Rowlands, Determining all displacements, strains and stresses full-field from measured values of a single displacement component, Exp. Mech. 54 (3) (2014) 443–455.
[54] A.A. Khaja, R.E. Rowlands, Experimentally determined stresses associated with elliptical holes using polar coordinates, Strain 49 (2) (2013) 116–124.
[55] W. Samad, R. Rowlands, Nondestructive full-field stress analysis of a finite structure containing an elliptical hole using digital image correlation, 2012, volume 12.
[56] W. Samad, R. Rowlands, Full-field thermoelastic stress analysis of a finite structure containing an irregularly-shaped hole, Exp. Mech. 54 (3) (2014) 457–469.
[57] S.-J.K. Lin, Two-and three-dimensional hybrid photomechanical-numerical stress analysis, 2007.
[58] W.A. Samad, R.E. Rowlands, Hybrid thermoelastic analysis of an unsymmetrically-loaded structure containing an arbitrarily-shaped cutout, in: Residual Stress, Thermomechanics and Infrared Imaging, Hybrid Techniques and Inverse Problems, Vol. 8, Springer, 2014, pp. 51–57.

[59] W. Samad, R. Rowlands, Individual stress determination in irregularly perforated unsymmetrically-loaded structures from temperature data, Aerosp. Sci. Technol. 63 (Supplement C) (2017) 91–99.
[60] W. Samad, A. Khaja, A. Kaliyanda, R. Rowlands, Hybrid thermoelastic stress analysis of a pinned joint, Exp. Mech. 54 (4) (2014) 515–525.
[61] S.-J. Lin, S. Quinn, D. Matthys, A. New, I. Kincaid, B. Boyce, A. Khaja, R. Rowlands, Thermoelastic determination of individual stresses in vicinity of a near-edge hole beneath a concentrated load, Exp. Mech. 51 (6) (2011) 797–814, Publisher: Springer US.
[62] S. Lin, D. Matthys, S. Quinn, J. Davidson, B. Boyce, A. Khaja, R. Rowlands, Stresses at and in the neighborhood of a near-edge hole in a plate subjected to an offset load from measured temperatures, Eur. J. Mech. A Solids 39 (2013) 209–217.
[63] B.E. Foust, J.R. Lesniak, R.E. Rowlands, Stress analysis of a pinned wood joint by grey-field photoelasticity, Composites B 61 (2014) 291–299.
[64] B. Kalaycioglu, A. Alshaya, R. Rowlands, Experimental stress analysis of an arbitrary geometry containing irregulary shaped hole, e12306, Strain 55 (3) (2019).
[65] B. Kalaycioglu, Stress analysis of an arbitrarily-shaped structure with an irregularly-shaped hole using digital image correlation, Mech. Mater. 147 (2020) 103415.
[66] T. Baek, R. Rowlands, Hybrid stress analysis of perforated composites using strain gages, Exp. Mech. 41 (2) (2001) 195–203.
[67] T.H. Baek, R.E. Rowlands, Experimental determination of stress concentrations in orthotropic composites, J. Strain Anal. Eng. Des. 34 (2) (1999) 69–81.
[68] J.S. Hawong, C.H. Lin, S.T. Lin, J. Rhee, R.E. Rowlands, A hybrid method to determine individual stresses in orthotropic composites using only measured isochromatic data, J. Compos. Mater. 29 (18) (1995) 2366–2387.
[69] J. Rhee, R. Rowlands, Thermoelastic-numerical hybrid analysis of holes and cracks in composites, Exp. Mech. 39 (4) (1999) 349–355.
[70] A. Alshaya, X. Shuai, R. Rowlands, Thermoelastic stress analysis of a finite orthotropic composite containing an elliptical hole, Exp. Mech. 56 (8) (2016) 1373–1384.
[71] A. Alshaya, S.-J. Lin, Hybrid stress analysis of a near-surface circular hole in finite structures, Proc. Inst. Mech. Eng. C 234 (7) (2019) 1366–1381, Publisher: IMECHE.
[72] R.B. Vieira, S. Kurunthottikkal Philip, G.L.G. Gonzáles, J.L. Freire, B. Yang, R.E. Rowlands, Determination of a U-notch stress concentration factor using thermoelasticity, J. Mech. Eng. Autom. 6 (2016) 66–76.
[73] A. Alshaya, J. Hunt, R. Rowlands, Stresses and strains in thick perforated orthotropic plates, J. Eng. Mech. 142 (11) (2016) 04016082.
[74] J. Dulieu-Smith, Alternative calibration techniques for quantitative thermoelastic stress analysis, Strain 31 (1) (1995) 9–16, Publisher: John Wiley & Sons, Ltd.
[75] A.A. Alshaya, Experimental, Analytical and Numerical Analyses of Orthotropic Materials and Biomechanics Application (Ph.D. thesis), University of Wisconsin-Madison, Madison, WI, USA, 2017.